

www.acsami.org Research Article

# Correlative Nanoscale Imaging of Strained hBN Spin Defects

David Curie, Jaron T. Krogel, Lukas Cavar, Abhishek Solanki, Pramey Upadhyaya, Tongcang Li, Yun-Yi Pai, Michael Chilcote, Vasudevan Iyer, Alexander Puretzky, Ilia Ivanov, Mao-Hua Du, Fernando Reboredo, and Benjamin Lawrie\*



Cite This: ACS Appl. Mater. Interfaces 2022, 14, 41361-41368



ACCESS

Metrics & More

Article Recommendations

Particle Recommendations

ABSTRACT: Spin defects like the negatively charged boron vacancy color center ( $V_B$ -) in hexagonal boron nitride (hBN) may enable new forms of quantum sensing with near-surface defects in layered van der Waals heterostructures. Here, the effect of strain on  $V_B$ - color centers in hBN is revealed with correlative cathodoluminescence and photoluminescence microscopies. Strong localized enhancement and redshifting of the  $V_B$ - luminescence is observed at creases, consistent with density functional theory calculations showing  $V_B$ - migration toward regions with moderate uniaxial compressive strain. The ability to manipulate spin defects with highly localized strain is critical to the development of practical 2D quantum devices and quantum sensors.

KEYWORDS: hBN, spin defects, cathodoluminescence, nanophotonics, quantum sensors

#### 1. INTRODUCTION

Color centers in hexagonal boron nitride (hBN) have drawn increasing interest since single-photon emission from hBN color centers was reported in 2016.<sup>1-4</sup> More recently, spin defects in hBN have drawn interest for applications in quantum sensing, quantum networking, and quantum computing.5-The development of new quantum technologies based on V<sub>B</sub>spin defects in hBN depends on improved understanding and control of the effect of the hBN environment on V<sub>B</sub>luminescence. Unfortunately, establishing links between atomic structures, nanoscale morphology, and mesoscale optical properties remains challenging. Transmission electron microscopes<sup>15</sup> and scanning tunneling microscopes<sup>16,17</sup> have been used to image and manipulate defects in hBN, but because (1) optically active defects are generally sparsely distributed, (2) high-energy electron beams can modify atomic defects, and (3) optical access in these microscopes is generally limited, correlating atomic and nanoscale structures with optical behavior remains a challenge. We have recently shown that multicolor photon correlation functions can be critical to understanding the correlations between different hBN photo-luminescence (PL) bands, 18,19 but additional research is needed to help accelerate basic research in quantum nanophotonics toward practical 2D quantum technologies.

 $V_B^-$  color centers have been patterned with ion beams,  $^{10,20}$  lasers,  $^{21}$  neutrons,  $^7$  and electron beams,  $^{22}$  and their photophysical properties are generally consistent with theory,  $^{23-26}$  although control over the defect distribution is still not well understood. While strain has proven to be a flexible tool for controlling single-photon emitters in hBN,  $^{26-31}$  many questions remain about the effect of strain on  $V_B^-$  color centers. Despite substantial recent progress,  $V_B^-$  PL exhibits poor quantum efficiency compared with more established optically accessible spin defects like the nitrogen vacancy (NV) center in diamond; there has still been no report of a single  $V_B^-$  defect emission.

Received: July 4, 2022 Accepted: August 24, 2022 Published: September 1, 2022





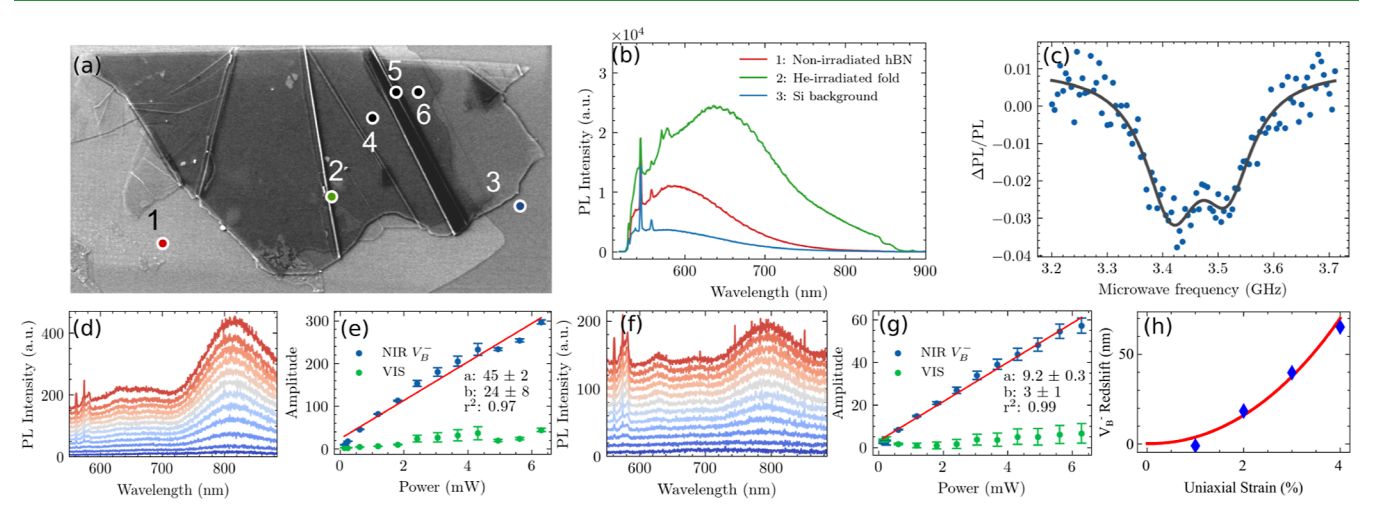


Figure 1. (a) 46.0 μm × 23.7 μm SEM image of a He-irradiated hBN flake. (b) PL spectra at positions 1, 2, and 3. (c) Continuous wave optically detected magnetic resonance (ODMR) spectrum acquired with a 700 nm long-pass filter at position 4. (d,e) Power-dependent PL on a crease at position 5 with associated Lorentz fit parameters. (f,g) Power-dependent PL at position 6 with associated Lorentz fit parameters. In (d) and (f), the power increases monotonically from blue to red from 0.13 to 6.3 mW. In (e) and (g), the fitted amplitude of the V<sub>B</sub>- luminescence is shown in blue, the fitted amplitude of the broadband visible luminescence is shown in green, and a linear fit to the V<sub>B</sub>- PL power dependence is included with fit parameters in the inset. A constant 10-unit offset is used between spectra in the waterfall plots in (d) and (f). (h) Density functional theory (DFT) calculations for the predicted redshift of V<sub>B</sub>- emission in the presence of uniaxial strain.

Cathodoluminescence (CL) microscopies have found increasing relevance in the characterization of color centers in hBN, with spatial resolution beyond the optical diffraction limit. 27,32,33 CL also offers additional opportunities to probe excitation and relaxation pathways that are not present in PL spectrum images (because the high-energy, near-field excitation is not constrained by far-field optical selection rules) and to correlate nanoscale morphology with device-scale optical properties. However, unlike PL microscopy, CL is not generally a useful tool for probing defect spin states. Furthermore, electron-beam interactions with matter are typically weak in the thin-flake limit. Increased electron-beam doses can result in beam-induced damage, while reduced doses yield small signals that are challenging to interpret. Moreover, defects in oxide substrates often exhibit bright CL that can swamp the CL signal from 2D flakes. Recent work used this background substrate CL to quantify nanoscale transmission through a flake,<sup>34</sup> although understanding the convolution of 2D material CL, substrate CL, and the effect of an exfoliated flake on the substrate CL can be challenging. Here, we reveal the effect of strain associated with creases in hBN flakes on V<sub>B</sub>color centers in hBN with non-negative matrix factorization (NMF)<sup>35</sup> of CL and PL spectrum images.

# 2. EXPERIMENTAL AND NUMERICAL METHODS

Ensemble defects were introduced into a hBN flake (~10-20 nm thick) by helium ion irradiation using a previously described method, 10 and the flake was transferred onto an un-irradiated hBN flake (that serves as a reference system with no extrinsic defects) on a 285 nm thick SiO<sub>2</sub> layer on a Si substrate, as shown in a scanning electron microscopy (SEM) image in Figure 1a.

Ambient PL microscopies were performed using a 532 nm continuous wave laser excitation and a 100× objective in order to provide a mesoscale understanding of the defect population in the flake after helium irradiation and in order to probe the ODMR spectrum of the V<sub>B</sub>- defect band near 800 nm. CL microscopy was performed on a FEI Quattro environmental scanning electron microscope with a Delmic Sparc CL collection module. The electron beam in the scanning electron microscope excites the sample through a pinhole in a parabolic mirror. The parabolic mirror collimates the

resulting CL for characterization with an Andor Kymera spectrometer, and the secondary electron (SE) signal is concurrently measured on an Everhart-Thornley detector. All CL spectrum images reported here were acquired at 5 keV in a 0.3 mbar water-vapor background. The electron beam was rastered within each pixel of the CL image during its measurement dwell time to generate a high-pixel-density concurrent SEM image. The electron beam in the SEM used here has a spot size of 0.7 nm in high vacuum that is increased to 2-3 nm at 5 keV in low vacuum. The CL spatial resolution is further constrained by free-carrier migration after electron-beam excitation, but CL still offers 1-2 orders of magnitude better spatial resolution than PL

A series of DFT calculations of strained V<sub>B</sub>- defects were performed to better understand the influence of strain on the V<sub>B</sub>- emission at the creases. The calculations were performed with the Quantum Espresso package  $^{36}$  with the PBE  $^{37,38}$  functional and ultrasoft GBRV  $^{39}$ pseudopotentials. Total energies were well converged with a planewave energy cutoff of 120 Ry. The V<sub>B</sub>- structure was represented in 239 atom periodic supercells with a  $2 \times 2 \times 2$  *k*-point grid. Relaxation of the local atomic structure was performed with the BFGS algorithm, with convergence tolerances of 1 meV for the total energy and 0.02 eV/Å for forces. All calculations were spin polarized, consistent with the triplet ground state of V<sub>B</sub>-.

### 3. RESULTS

Several spectral features are immediately visible in hyperspectral PL maps of the flake and illustrated in point spectra shown in Figure 1b,d,f. Figure 1b illustrates typical PL point spectra from the bare substrate, from un-irradiated hBN, and from one position on helium-irradiated hBN. Silicon and hBN Raman lines and broad defect luminescence bands are visible in each. The V<sub>B</sub>- emission appears as a shoulder at wavelengths near 800 nm in the PL spectrum acquired at position 2, but it is not present as a distinct well-resolved peak at all positions on the flake.

Increased V<sub>B</sub>⁻ PL is seen at wavelengths of ~750−900 nm at positions 5 and 6 in Figure 1a. The power-dependent PL measured at those sites is plotted in Figure 1d,f. An ODMR spectrum acquired at position 4 with a 750 nm long-pass filter (shown in Figure 1c) exhibits moderate contrast of almost 4%, confirming the presence of ensemble V<sub>B</sub>- defects. The

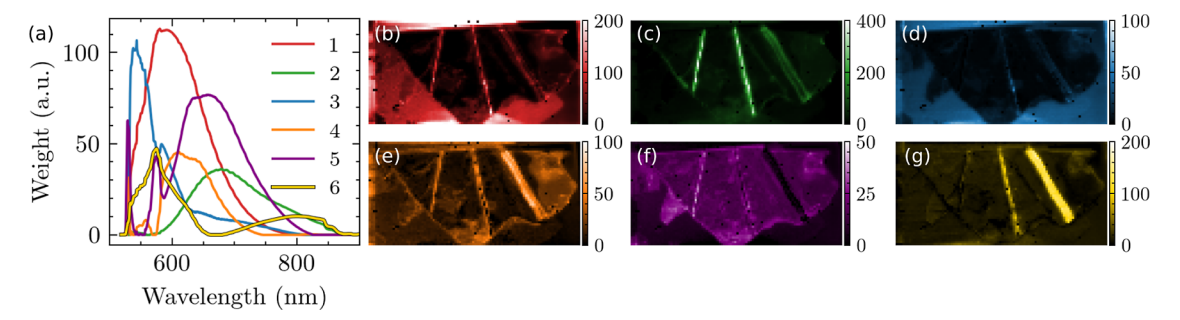


Figure 2. NMF decomposition of the hyperspectral PL map of the same He-irradiated hBN flake shown in Figure 1. Spectral components illustrated in (a) are color coded to the six associated NMF maps in (b-g).

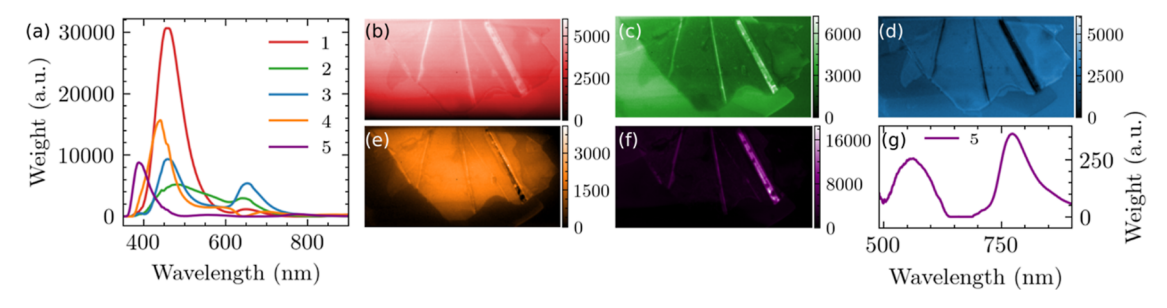


Figure 3. NMF decomposition of a hyperspectral CL map of the same He-irradiated hBN flake shown in Figure 1. (a) NMF spectral components corresponding to their color-coded spatial maps in (b-f). (g) NMF spectral component 5 from 500 to 900 nm (highlighting the weak emission at 560 and 790 nm).

wavelength and amplitude of the PL spectra in Figure 1d,f were fitted to two Lorentzians; the fitted amplitude parameters are plotted as a function of excitation laser power in Figure 1e,g, with linear fits to the  $V_{B^-}$  power dependence included in each graph.

Notably, the relative intensity of the  $V_B^-$  PL is highly heterogeneous, and the  $V_B^-$  energy redshifts by  $\sim 30$  nm in the presence of strain at the crease. In addition, the  $V_B^-$  PL intensity grows much more quickly with increasing laser power than the visible PL, and the  $V_B^-$  PL intensity grows much more quickly on the crease than off the crease. Linear least-squares fits to the power-dependent PL amplitude plotted in Figure 1e,g show a slope that is  $\sim 5\times$  larger for  $V_B^-$  PL on the crease than off the crease. The relatively weak signal at visible wavelengths at positions 5 and 6 limits the quality of the fit to the visible luminescence, but the difference in scaling of the visible and  $V_B^-$  PL on and off the crease is clear. The linewidths and central wavelengths of the fits showed no statistically significant dependence on excitation power.

The heterogeneity of the  $V_B$ - PL is illustrated in Figure 2, which shows the NMF decomposition of a PL spectrum image of the same flake acquired with a 2.2 mW laser excitation. NMF is a popular, computationally inexpensive tool for extracting sparse, physically relevant data from hyperspectral data sets that assume that a spectrum image results from the linear combination of non-negative constituent spectra. The PL component 1 in Figure 2a,b has a peak at 600 nm that is consistent with the un-irradiated background hBN PL spectrum in Figure 1b, and it exhibits a strong spatial correlation with the un-irradiated hBN. Likewise, PL component 3 in Figure 2a,d is consistent with the measured substrate luminescence.

There is a clear positive correlation between the creases and the amplitude of PL components 2, 4, and 6. PL component 6 comprises the  $V_B^-$  PL band centered near 800 nm along with

correlated visible emission near 560 nm, and it is strongly enhanced by two of the creases in the flake, as seen in Figure 2g. PL components 2 and 4 comprise visible emission bands that are also enhanced at creases in the flake, as seen in Figure 2c,e. PL component 2 may include  $V_{B^-}$  PL in the shoulder of a higher energy peak, although it is not as well resolved as the  $V_{B^-}$  band in component 6. PL component 5 is strongly spatially correlated with the He-irradiated hBN flake, but it is attenuated at the creases, and it shows no emission at the  $V_{B^-}$  PL band near 800 nm. The origin of the spatial heterogeneity of the hBN PL is discussed below.

A rastered CL spectrum image of the same flake was acquired using a beam current of 1800 pA, a step size of 400 nm, and a dwell time of 600 ms per pixel. The NMF decomposition of that CL spectrum image is illustrated in Figure 3. CL components 1 and 3 in Figure 3a,b,d are consistent with the substrate luminescence, 34 and CL component 2 in Figure 3a,c is spatially correlated with the un-irradiated flake and can likely be attributed to intrinsic defect CL from that flake. Like PL component 5, CL component 4 is present across the He-irradiated hBN flake but attenuated at the creases, and it exhibits negligible intensity near 800 nm. CL component 5 exhibits weak luminescence bands centered near 790, 560, and 400 nm, as seen in the magnified low-energy portion of CL component 5 in Figure 3g. It is strongly enhanced by one of the largest creases on the flake with weaker enhancement at the other creases. The correlation between emission at 790 and 560 nm is consistent with the crease-enhanced luminescence in PL component 6. The bright emission at 400 nm that is spatially correlated with the defect bands at 790 and 560 nm in CL component 5 has not been previously reported in the literature.

Because the total measurement time and electron-beam dose scale as the inverse square of the step size, spectrum images utilizing step sizes much smaller than 400 nm are problematic

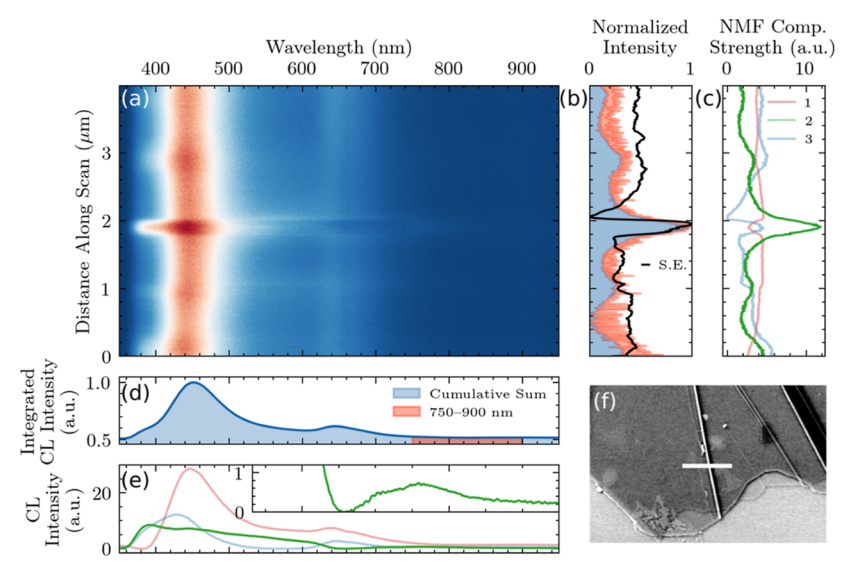


Figure 4. 4  $\mu$ m long CL linescan (a) was acquired across the white line in the SEM image (f). (b) Normalized panchromatic CL intensity as a function of the linescan position (blue) with normalized SE counts (black) and the normalized counts across the V<sub>B</sub>- band (red). (d) Integrated spectra across all linescan positions (blue) with the V<sub>B</sub>- band highlighted (red). (c,e) NMF decomposition of linescan with magnified low energy values for component 2 shown in the inset of (e). Wavelength axis is shared in (a,d,e), and linescan distance axis is shared in (a-c).

for flakes this large, but linescans that focus on individual features with higher spatial resolutions can still be performed quickly. A CL linescan was acquired using a beam current of 1 nA, a 100 ms dwell time, and a 5 nm step size, as illustrated in Figure 4. The spectrum image is dominated by a defect band near 450 nm, just as the spectrum image in Figure 3 is. The crease is identified in the CL linescan by the sudden enhancement in intensity in Figure 4a,b and the increased SE signal in Figure 4b. However, it is not immediately clear from Figure 4b how individual defect classes contribute to the enhanced emission at the crease. Just as NMF decomposition of a spectrum image enabled the extraction of spatially correlated spectral components in Figures 2 and 3, NMF decomposition of this linescan (illustrated in Figure 4c,e) can be used to extract weak spatially correlated defect bands. CL component 2 in Figure 4e exhibits weak emission around 750– 850 nm and correlated emission in the visible, and it is strongly enhanced on the crease, as evident in Figure 4c. CL components 1 and 3 exhibit a moderate change in intensity near the crease, but they are not strongly positively correlated with the crease position and the SE signal like component 2.

The number of components in each NMF reconstruction was chosen by monitoring the reconstruction error as a function of component number. The PL and CL NMF decompositions require a different number of components because of the different relaxation pathways available under electron and laser excitations. Similarly, a reduced number of components were required for the linescan because the reduced scan area introduced fewer spatially correlated components.

Critically, the NMF decompositions in Figures 2–4 illustrate selective enhancement of certain spectral components rather than uniformly enhanced luminescence at the creases. Thus, the enhancement is not simply a result of increased interaction volume at the crease (which would uniformly enhance all unsaturated defect luminescence). Instead, it is logical to consider the effect of strain at the crease on defect luminescence. Following He-ion bombardment, large populations of  $V_{\rm B}^-$ ,  $V_{\rm B}^0$ , and nitrogen vacancy  $(V_{\rm N})$  defects

(including various charge states) are expected to be present in the material with roughly comparable densities. According to previous DFT calculations, the creased regions attract both  $V_{\rm B}$  and  $V_{\rm N}$  defect species, as the formation energies of these defects are lowered with the increasing curvature of hBN. As

#### 4. DISCUSSION

Early first-principles calculations predicted  $V_B$  luminescence at 2.3 and 2.8 eV<sup>44</sup> under the electron—hole recombination conditions that are possible in CL. Similarly, DFT studies of charged  $V_N$  defects have predicted transition energies of 2–3 eV.<sup>44–46</sup> Moreover, CL microscopies of NV centers in diamond have shown that the electron beam converts the negatively charged NV center to the neutral NV center. This beam-induced charge-state conversion substantially changes the defect photophysics. Similar charge-state conversion likely occurs for the hBN defects probed here, which may explain the relative brightness of the  $V_B^-$  PL band compared to the  $V_B^-$  CL band. It is thus possible that the CL bands at 400 and 560 nm in NMF component 5 in Figure 3 may be associated with  $V_B^{\ 0}$  or other  $V_B$  charge states, although this claim is somewhat speculative at this stage.

Although both  $V_B$  and  $V_N$  species are attracted to creases, a strong asymmetry exists between the mobility of  $V_B$  and  $V_N$ . The migration barrier of  $V_N$  is very large, effectively inhibiting its motion, while the barrier for  $V_B$  migration is substantially lower, <sup>49</sup> enabling much greater mobility. The mobile  $V_B$  and  $V_B$ - species are therefore predicted to preferentially collect at creases in hBN, resulting in enhanced PL and CL in the 750–850 nm range at the creases driven by enhanced local populations of  $V_B$ - defects in those regions. An increased density of  $V_B$ - defects at creases is also consistent with the increased slope seen in the power-dependent PL plotted in Figure 1e.

The local strain environment at the creases may also contribute to changes in  $V_{B^-}$  emission relative to the pristine and locally flat regions. Computational studies of hBN nanotubes have shown that the tubes constrict along the axial direction relative to pure hBN,  $^{50-52}$  indicating a roughly

uniaxial compressive strain at the creases. Thus, we consider only compressive strain in our calculations. DFT calculations performed in this work for V<sub>B</sub>- defects under uniaxial compressive strain show a modest redshift in the primary emission line of V<sub>B</sub>- as the strain is increased, as shown in Figure 1h, where leave-one-out cross-validation has been used to reduce small numerical fluctuations in the band gap fits. Based on these calculations, we find that a uniaxial strain of approximately 2.5% is sufficient to explain the observed 30 nm redshift in the PL spectra at the creases relative to the unstrained regions. While the assumption of uniaxial compressive strain is likely an over-simplification due to the thickness of the flake, the prediction of redshift should persist even in the variable curvature environment at the crease. However, we should note that we were not able to experimentally quantify the depth profile of the V<sub>B</sub>- defects in the flake directly.

Notably, the NMF algorithm used here is an example of "blind" spectral unmixing. In other words, no assumptions were made about the structure of each spectral component. The presence of at least two electronic transitions in a given NMF component does not necessarily suggest that a single defect is responsible for multiple transitions, but it does suggest that all electronic transitions in each component are spatially correlated with one another. The bands centered near 800 nm in PL component 6 and CL component 5 in Figures 2 and 3, respectively, are consistent with V<sub>B</sub>- luminescence, and the ODMR spectrum shown in Figure 1c corroborates this assignment. However, most models of V<sub>B</sub>- luminescence suggest that it has only a single optically active transition centered near  $800\,$  nm.  $^{53}$  Because helium irradiation should create comparable densities of  $V_B$  and  $V_{B^-}$ , because these defects should exhibit comparable mobility, because of the first-principles calculations that have described V<sub>B</sub> luminescence,<sup>44</sup> and because of the possibility of electron beaminduced charge-state conversion, it seems reasonable to conclude that the transition at 570 nm in PL component 6 and the transitions at 550 and 400 nm in CL component 5 are a result of V<sub>B</sub> luminescence. Because PL component 2 exhibits a large shoulder at 800 nm and exhibits substantial strain enhancement at each of the creases, it similarly seems reasonable to assign PL component 2 to a higher energy V<sub>B</sub> transition with spatially correlated V<sub>B</sub>- luminescence.

The luminescence in PL components 4 and 5 and CL component 4 in Figures 2 and 3, respectively, is not strongly correlated with the V<sub>B</sub>- band near 800 nm, and thus it seems unlikely that they are V<sub>B</sub>- luminescence bands. Based on the understanding that helium irradiation should generate a moderate density of V<sub>N</sub> defects with reduced mobility compared with  $V_{B^{\text{-}}}$  and  $V_{B^{\text{+}}}$  PL component 5 and  $\stackrel{\cdot}{\text{CL}}$ component 4, which exhibit roughly uniform luminescence across the flake, can be assigned to V<sub>N</sub> luminescence. CL component 4 also exhibits strong emission near 460 nm, which corresponds closely to the onset of photo-current observed in prior optical absorption measurements of hBN. 54 It is therefore possible to interpret this peak, which has broad spatial coverage over the sample, as being associated with the photo-ionization of V<sub>N</sub>, leading to the production of free carriers.

Despite the strong correlations between the PL and CL NMF decompositions, there are some visible distinctions between the spectral components. There are a few reasons for this: (1) most critically, PL microscopy relies on a below-band

gap excitation, but the electron beam excites electrons to the conduction band, resulting in the emergence of additional decay pathways that are not present in PL (and the PL map includes Raman modes that are not present in CL). (2) Many defect classes in hBN are sensitive to electron-beam excitation. While the electron-beam doses that we used here did not visibly damage the hBN flake, it is possible that beam-induced damage introduced additional defects or quenched existing defects during the measurement. (3) Electron beam-induced charge-state conversion has not been previously reported in hBN, but based on comparable physics observed for NV centers in diamond, it is possible that some beam-induced charge-state conversion is present in these data. However, these distinctions are not necessarily impediments to the nanoscale mapping of spin defect properties near creases in hBN. Indeed, the variation between PL and CL spectral components provides a richer understanding of the defect photophysics than can be extracted from a single measurement modality by itself.

#### 5. CONCLUSIONS

CL microscopies have not seen widespread use in the characterization of thin 2D materials because small-interaction cross-sections limit the measurement efficiency. The spectral decomposition of CL spectrum images used here provides a more complete picture of the effect of flake morphology on correlated spectral components with a spatial resolution of order 5 nm. A clear understanding of the nanophotonic properties of  $V_{B^-}$  defects in hBN is essential to the development of 2D quantum sensors. Atomically thin quantum sensors could offer improved sensitivity compared with bulk diamond-based sensors, and 2D materials are easier to integrate into devices. However, V<sub>B</sub>- luminescence remains very weak compared with NV center luminescence. The straininduced migration of V<sub>B</sub>- defects into intrinsic creases in hBN flakes that we have described here is one critical path toward addressing this obstacle.

# AUTHOR INFORMATION

#### Corresponding Author

Benjamin Lawrie – Materials Science and Technology Division, Oak Ridge National Laboratory, Oak Ridge, Tennessee 37831, United States; Quantum Science Center, Oak Ridge, Tennessee 37831, United States; oorcid.org/ 0000-0003-1431-066X; Email: lawriebj@ornl.gov

#### Authors

**David Curie** – Department of Physics and Astronomy, Vanderbilt University, Nashville, Tennessee 37235, United

Jaron T. Krogel – Materials Science and Technology Division, Oak Ridge National Laboratory, Oak Ridge, Tennessee 37831, United States; orcid.org/0000-0002-1859-181X

Lukas Cavar - Department of Physics, Indiana University, Bloomington, Indiana 47405, United States

Abhishek Solanki - Elmore Family School of Electrical and Computer Engineering, Purdue University, West Lafayette, Indiana 47907, United States

Pramey Upadhyaya – Elmore Family School of Electrical and Computer Engineering, Purdue University, West Lafayette, Indiana 47907, United States

Tongcang Li - Elmore Family School of Electrical and Computer Engineering, Purdue University, West Lafayette,

- Indiana 47907, United States; Department of Physics and Astronomy, Purdue University, West Lafayette, Indiana 47907, United States; orcid.org/0000-0003-3308-8718
- Yun-Yi Pai Materials Science and Technology Division, Oak Ridge National Laboratory, Oak Ridge, Tennessee 37831, United States; Quantum Science Center, Oak Ridge, Tennessee 37831, United States; oorcid.org/0000-0003-2251-0231
- Michael Chilcote Materials Science and Technology Division, Oak Ridge National Laboratory, Oak Ridge, Tennessee 37831, United States; Quantum Science Center, Oak Ridge, Tennessee 37831, United States
- Vasudevan Iyer Center for Nanophase Materials Sciences, Oak Ridge National Laboratory, Oak Ridge, Tennessee 37831, United States
- Alexander Puretzky Center for Nanophase Materials Sciences, Oak Ridge National Laboratory, Oak Ridge, Tennessee 37831, United States; oorcid.org/0000-0002-9996-4429
- Ilia Ivanov Center for Nanophase Materials Sciences, Oak Ridge National Laboratory, Oak Ridge, Tennessee 37831, United States; o orcid.org/0000-0002-6726-2502
- Mao-Hua Du Materials Science and Technology Division, Oak Ridge National Laboratory, Oak Ridge, Tennessee 37831, United States; orcid.org/0000-0001-8796-167X
- Fernando Reboredo Materials Science and Technology Division, Oak Ridge National Laboratory, Oak Ridge, Tennessee 37831, United States

Complete contact information is available at: https://pubs.acs.org/10.1021/acsami.2c11886

# Notes

The authors declare no competing financial interest.

# ACKNOWLEDGMENTS

This research was sponsored by the U. S. Department of Energy, Office of Science, Basic Energy Sciences, Materials Sciences and Engineering Division. The PL and CL microscopies were performed at the Center for Nanophase Materials Sciences, which is a U.S. Department of Energy Office of Science User Facility. Sample preparation was supported by the DARPA QUEST Program and by the U.S. Department of Energy, Office of Science, National Quantum Information Science Research Centers, Quantum Science Center. Student support was provided by the U.S. Department of Energy, Office of Science, Office of Workforce Development for Teachers and Scientists, Office of Science Graduate Student Research (SCGSR) program, and by NSF award DMR-1747426. The SCGSR program is administered by the Oak Ridge Institute for Science and Education for the DOE under contract number DE-SC0014664. This research used resources of the Compute and Data Environment for Science (CADES) at the Oak Ridge National Laboratory, which is supported by the Office of Science of the U.S. Department of Energy under Contract no. DE-AC05-00OR22725. The authors would like to acknowledge Vladimir Shalaev for ODMR spectroscopy support. This manuscript has been authored by UT-Battelle, LLC, under contract DE-AC05-00OR22725 with the US Department of Energy (DOE). The US government retains and the publisher, by accepting the article for publication, acknowledges that the US government retains a nonexclusive, paid-up, irrevocable, worldwide license

to publish or reproduce the published form of this manuscript, or allow others to do so, for US government purposes. DOE will provide public access to these results of federally sponsored research in accordance with the DOE Public Access Plan (http://energy.gov/downloads/doe-public-access-plan).

#### REFERENCES

- (1) Tran, T. T.; Elbadawi, C.; Totonjian, D.; Lobo, C. J.; Grosso, G.; Moon, H.; Englund, D. R.; Ford, M. J.; Aharonovich, I.; Toth, M. Robust Multicolor Single Photon Emission from Point Defects in Hexagonal Boron Nitride. ACS Nano 2016, 10, 7331-7338.
- (2) Aharonovich, I.; Englund, D.; Toth, M. Solid-State Single-Photon Emitters. Nat. Photonics 2016, 10, 631-641.
- (3) Tran, T. T.; Bray, K.; Ford, M. J.; Toth, M.; Aharonovich, I. Quantum Emission from Hexagonal Boron Nitride Monolayers. Nat. Nanotechnol. 2016, 11, 37-41.
- (4) Martínez, L. J.; Pelini, T.; Waselowski, V.; Maze, J. R.; Gil, B.; Cassabois, G.; Jacques, V. Efficient Single Photon Emission from a High-Purity Hexagonal Boron Nitride Crystal. Phys. Rev. B 2016, 94,
- (5) Stern, H. L.; Gu, J.; Jarman, Q.; Eizagirre Barker, S. E.; Mendelson, N.; Chugh, D.; Schott, S.; Tan, H. H.; Sirringhaus, H.; Aharonovich, I.; Atatüre, M. Room-Temperature Optically Detected Magnetic Resonance of Single Defects in Hexagonal Boron Nitride. Nat. Commun. 2022, 13, 618.
- (6) Auburger, P.; Gali, A. Towards Ab Initio Identification of Paramagnetic Substitutional Carbon Defects in Hexagonal Boron Nitride Acting as Quantum Bits. Phys. Rev. B 2021, 104, 075410.
- (7) Gottscholl, A.; Diez, M.; Soltamov, V.; Kasper, C.; Sperlich, A.; Kianinia, M.; Bradac, C.; Aharonovich, I.; Dyakonov, V. Room Temperature Coherent Control of Spin Defects in Hexagonal Boron Nitride. Sci. Adv. 2021, 7, No. eabf3630.
- (8) Baber, S.; Malein, R. N. E.; Khatri, P.; Keatley, P. S.; Guo, S.; Withers, F.; Ramsay, A. J.; Luxmoore, I. J. Excited State Spectroscopy of Boron Vacancy Defects in Hexagonal Boron Nitride Using Time-Resolved Optically Detected Magnetic Resonance. Nano Lett. 2021,
- (9) Gottscholl, A.; Kianinia, M.; Soltamov, V.; Orlinskii, S.; Mamin, G.; Bradac, C.; Kasper, C.; Krambrock, K.; Sperlich, A.; Toth, M.; Aharonovich, I.; Dyakonov, V. Initialization and Read-Out of Intrinsic Spin Defects in a van der Waals Crystal at Room Temperature. Nat. Mater. 2020, 19, 540-545.
- (10) Kianinia, M.; White, S.; Fröch, J. E.; Bradac, C.; Aharonovich, I. Generation of Spin Defects in Hexagonal Boron Nitride. ACS Photonics 2020, 7, 2147-2152.
- (11) Mathur, N.; Mukherjee, A.; Gao, X.; Luo, J.; McCullian, B. A.; Li, T.; Vamivakas, A. N.; Fuchs, G. D. Excited-State Spin-Resonance Spectroscopy of VB- Defect Centers in Hexagonal Boron Nitride. Nat. Commun. 2022, 13, 3233.
- (12) Murzakhanov, F. F.; Mamin, G. V.; Orlinskii, S. B.; Gerstmann, U.; Schmidt, W. G.; Biktagirov, T.; Aharonovich, I.; Gottscholl, A.; Sperlich, A.; Dyakonov, V.; Soltamov, V. Electron-Nuclear Coherent Coupling and Nuclear Spin Readout through Optically Polarized VB-Spin States in hBN. Nano Lett. 2022, 22, 2718-2724.
- (13) Mu, Z.; Cai, H.; Chen, D.; Kenny, Z.; Jiang, S.; Ru, X.; Lyu, X.; Koh, I.; Liu, W.; Aharonovich, I.; Gao, W. Excited-State Optically Detected Magnetic Resonance of Spin Defects in Hexagonal Boron Nitride. Phys. Rev. Lett. 2022, 128, 216402.
- (14) Tetienne, J.-P. Quantum Sensors Go Flat. Nat. Phys. 2021, 17, 1074-1075.
- (15) Jin, C.; Lin, F.; Suenaga, K.; Iijima, S. Fabrication of a Freestanding Boron Nitride Single Layer and its Defect Assignments. Phys. Rev. Lett. 2009, 102, 195505.
- (16) Qiu, Z.; Vaklinova, K.; Huang, P.; Grzeszczyk, M.; Yang, H.; Watanabe, K.; Taniguchi, T.; Novoselov, K.; Lu, J.; Koperski, M. Atomic Structure of Carbon Centres in hBN: Towards Engineering of Single Photon Sources. 2021, arXiv:2110.07842 cond-mat.mtrl-sci Submitted on 15 Oct 2021.

- (17) Wong, D.; Velasco, J.; Ju, L.; Lee, J.; Kahn, S.; Tsai, H.-Z.; Germany, C.; Taniguchi, T.; Watanabe, K.; Zettl, A.; Wang, F.; Crommie, M. Characterization and Manipulation of Individual Defects in Insulating Hexagonal Boron Nitride Using Scanning Tunnelling Microscopy. Nat. Nanotechnol. 2015, 10, 949-953.
- (18) Feldman, M. A.; Marvinney, C. E.; Puretzky, A. A.; Lawrie, B. J. Evidence of Photochromism in a Hexagonal Boron Nitride Single-Photon Emitter. Optica 2021, 8, 1-5.
- (19) Feldman, M. A.; Puretzky, A.; Lindsay, L.; Tucker, E.; Briggs, D. P.; Evans, P. G.; Haglund, R. F.; Lawrie, B. J. Phonon-Induced Multicolor Correlations in hBN Single-Photon Emitters. Phys. Rev. B 2019, 99, 020101.
- (20) Gao, X.; Jiang, B.; Llacsahuanga Allcca, A. E.; Shen, K.; Sadi, M. A.; Solanki, A. B.; Ju, P.; Xu, Z.; Upadhyaya, P.; Chen, Y. P.; Bhave, S. A.; Li, T. High-Contrast Plasmonic-Enhanced Shallow Spin Defects in Hexagonal Boron Nitride for Quantum Sensing. Nano Lett. 2021, 21, 7708-7714.
- (21) Gao, X.; Pandey, S.; Kianinia, M.; Ahn, J.; Ju, P.; Aharonovich, I.; Shivaram, N.; Li, T. Femtosecond Laser Writing of Spin Defects in Hexagonal Boron Nitride. ACS Photonics 2021, 8, 994-1000.
- (22) Murzakhanov, F. F.; Yavkin, B. V.; Mamin, G. V.; Orlinskii, S. B.; Mumdzhi, I. E.; Gracheva, I. N.; Gabbasov, B. F.; Smirnov, A. N.; Davydov, V. Y.; Soltamov, V. A. Creation of Negatively Charged Boron Vacancies in Hexagonal Boron Nitride Crystal by Electron Irradiation and Mechanism of Inhomogeneous Broadening of Boron Vacancy-Related Spin Resonance Lines. Nanomaterials 2021, 11,
- (23) Abdi, M.; Chou, J.-P.; Gali, A.; Plenio, M. B. Color Centers in Hexagonal Boron Nitride Monolayers: A Group Theory and Ab Initio Analysis. ACS Photonics 2018, 5, 1967-1976.
- (24) Libbi, F.; de Melo, P. M. M. C.; Zanolli, Z.; Verstraete, M.; Marzari, N. Phonon-Assisted Luminescence in Defect Centers from Many-Body Perturbation Theory. Phys. Rev. Lett. 2022, 128, 167401.
- (25) Chen, Y.; Quek, S. Y. Photophysical Characteristics of Boron Vacancy-Derived Defect Centers in Hexagonal Boron Nitride. J. Phys. Chem. C 2021, 125, 21791-21802.
- (26) Li, S.; Chou, J.-P.; Hu, A.; Plenio, M. B.; Udvarhelyi, P.; Thiering, G.; Abdi, M.; Gali, A. Giant Shift Upon Strain on the Fluorescence Spectrum of  $V_N N_B$  Color Centers in h-BN. npj Quantum Inf. 2020, 6, 85.
- (27) Hayee, F.; Yu, L.; Zhang, J. L.; Ciccarino, C. J.; Nguyen, M.; Marshall, A. F.; Aharonovich, I.; Vučković, J.; Narang, P.; Heinz, T. F.; Dionne, J. Revealing Multiple Classes of Stable Quantum Emitters in Hexagonal Boron Nitride with Correlated Optical and Electron microscopy. Nat. Mater. 2020, 19, 534-539.
- (28) Deng, S.; Sumant, A. V.; Berry, V. Strain Engineering in Two-Dimensional Nanomaterials Beyond Graphene. Nano Today 2018, 22,
- (29) Mendelson, N.; Doherty, M.; Toth, M.; Aharonovich, I.; Tran, T. T. Strain-Induced Modification of the Optical Characteristics of Quantum Emitters in Hexagonal Boron Nitride. Adv. Mater. 2020, 32, 1908316.
- (30) Proscia, N. V.; Shotan, Z.; Jayakumar, H.; Reddy, P.; Cohen, C.; Dollar, M.; Alkauskas, A.; Doherty, M.; Meriles, C. A.; Menon, V. M. Near-Deterministic Activation of Room-Temperature Quantum Emitters in Hexagonal Boron Nitride. Optica 2018, 5, 1128-1134.
- (31) Yim, D.; Yu, M.; Noh, G.; Lee, J.; Seo, H. Polarization and Localization of Single-Photon Emitters in Hexagonal Boron Nitride Wrinkles. ACS Appl. Mater. Interfaces 2020, 12, 36362-36369.
- (32) Bourrellier, R.; Meuret, S.; Tararan, A.; Stéphan, O.; Kociak, M.; Tizei, L. H.; Zobelli, A. Bright UV Single Photon Emission at Point Defects in h-BN. Nano Lett. 2016, 16, 4317-4321.
- (33) Meuret, S.; Tizei, L.; Cazimajou, T.; Bourrellier, R.; Chang, H.; Treussart, F.; Kociak, M. Photon Bunching in Cathodoluminescence. Phys. Rev. Lett. 2015, 114, 197401.
- (34) Negri, M.; Francaviglia, L.; Dumcenco, D.; Bosi, M.; Kaplan, D.; Swaminathan, V.; Salviati, G.; Kis, A.; Fabbri, F.; Fontcuberta i Morral, A. Quantitative Nanoscale Absorption Mapping: A Novel

- Technique To Probe Optical Absorption of Two-Dimensional Materials. Nano Lett. 2020, 20, 567-576.
- (35) Wang, Y.-X.; Zhang, Y.-J. Nonnegative Matrix Factorization: A Comprehensive Review. IEEE Trans. Knowl. Data Eng. 2013, 25,
- (36) Giannozzi, P.; Baroni, S.; Bonini, N.; Calandra, M.; Car, R.; Cavazzoni, C.; Ceresoli, D.; Chiarotti, G. L.; Cococcioni, M.; Dabo, I.; Dal Corso, A.; de Gironcoli, S.; Fabris, S.; Fratesi, G.; Gebauer, R.; Gerstmann, U.; Gougoussis, C.; Kokalj, A.; Lazzeri, M.; Martin-Samos, L.; Marzari, N.; Mauri, F.; Mazzarello, R.; Paolini, S.; Pasquarello, A.; Paulatto, L.; Sbraccia, C.; Scandolo, S.; Sclauzero, G.; Seitsonen, A. P.; Smogunov, A.; Umari, P.; Wentzcovitch, R. M. QUANTUM ESPRESSO: a Modular and Open-Source Software Project for Quantum Simulations of Materials. J. Phys.: Condens. Matter 2009, 21, 395502.
- (37) Perdew, J. P.; Burke, K.; Ernzerhof, M. Generalized Gradient Approximation Made Simple. Phys. Rev. Lett. 1996, 77, 3865.
- (38) Perdew, J. P.; Burke, K.; Ernzerhof, M. Generalized Gradient Approximation Made Simple [Phys. Rev. Lett. 77, 3865 (1996)]. Phys. Rev. Lett. 1997, 78, 1396.
- (39) Garrity, K. F.; Bennett, J. W.; Rabe, K. M.; Vanderbilt, D. Pseudopotentials for High-Throughput DFT Calculations. Comput. Mater. Sci. 2014, 81, 446-452.
- (40) Iyer, V.; Phang, Y. S.; Butler, A.; Chen, J.; Lerner, B.; Argyropoulos, C.; Hoang, T.; Lawrie, B. Near-Field Imaging of Plasmonic Nanopatch Antennas with Integrated Semiconductor Quantum Dots. APL Photonics 2021, 6, 106103.
- (41) Liu, X.-Y.; Guo, S.; Ramoji, A.; Bocklitz, T.; Rösch, P.; Popp, J.; Yu, H.-Q. Spatiotemporal Organization of Biofilm Matrix Revealed by Confocal Raman Mapping Integrated with non-Negative Matrix Factorization Analysis. Anal. Chem. 2019, 92, 707-715.
- (42) Gu, R.; Wang, L.; Zhu, H.; Han, S.; Bai, Y.; Zhang, X.; Li, B.; Qin, C.; Liu, J.; Guo, G.; Shan, X.; Xiong, G.; Gao, J.; He, C.; Han, Z.; Liu, X.; Zhao, F. Engineering and Microscopic Mechanism of Quantum Emitters Induced by Heavy Ions in hBN. ACS Photonics 2021, 8, 2912-2922.
- (43) Zobelli, A.; Ewels, C. P.; Gloter, A.; Seifert, G.; Stephan, O.; Csillag, S.; Colliex, C. Defective Structure of BN Nanotubes: From Single Vacancies to Dislocation Lines. Nano Lett. 2006, 6, 1955-1960.
- (44) Huang, B.; Lee, H. Defect and Impurity Properties of Hexagonal Boron Nitride: A First-Principles Calculation. Phys. Rev. B: Condens. Matter Mater. Phys. 2012, 86, 245406.
- (45) Moon, C.-Y.; Hong, K.-S.; Kim, Y.-S. Analogous Atomic and Electronic Properties between V N and V N C B Defects in Hexagonal Boron Nitride. Adv. Condens. Matter Phys. 2022, 2022,
- (46) Sajid, A.; Reimers, J. R.; Ford, M. J. Defect States in Hexagonal Boron Nitride: Assignments of Observed Properties and Prediction of Properties Relevant to Quantum Computation. Phys. Rev. B 2018, 97,
- (47) Solà-Garcia, M.; Meuret, S.; Coenen, T.; Polman, A. Electron-Induced State Conversion in Diamond NV Centers Measured with Pump-Probe Cathodoluminescence Spectroscopy. ACS Photonics 2019, 7, 232-240.
- (48) Feldman, M. A.; Dumitrescu, E. F.; Bridges, D.; Chisholm, M. F.; Davidson, R. B.; Evans, P. G.; Hachtel, J. A.; Hu, A.; Pooser, R. C.; Haglund, R. F.; Lawrie, B. J. Colossal Photon Bunching in Quasiparticle-Mediated Nanodiamond Cathodoluminescence. Phys. Rev. B 2018, 97, No. 081404(R).
- (49) Zobelli, A.; Ewels, C. P.; Gloter, A.; Seifert, G. Vacancy Migration in Hexagonal Boron Nitride. Phys. Rev. B: Condens. Matter Mater. Phys. 2007, 75, 094104.
- (50) Blase, X.; Rubio, A.; Louie, S. G.; Cohen, M. L. Stability and Band Gap Constancy of Boron Nitride Nanotubes. Europhys. Lett. **1994**, 28, 335-340.
- (51) Jhi, S.-H.; Roundy, D. J.; Louie, S. G.; Cohen, M. L. Formation and Electronic Properties of Double-Walled Boron Nitride Nanotubes. Solid State Commun. 2005, 134, 397-402.

- (52) Chen, Y. K.; Liu, L. V.; Wang, Y. A. Density Functional Study of Interaction of Atomic Pt with Pristine and Stone-Wales-Defective Single-Walled Boron Nitride Nanotubes. J. Phys. Chem. C 2010, 114, 12382-12388.
- (53) Ivády, V.; Barcza, G.; Thiering, G.; Li, S.; Hamdi, H.; Chou, J.-P.; Legeza, Ö.; Gali, A. Ab Initio Theory of the Negatively Charged Boron Vacancy Qubit in Hexagonal Boron Nitride. npj Comput. Mater. 2020, 6, 41.
- (54) Remes, Z.; Nesladek, M.; Haenen, K.; Watanabe, K.; Taniguchi, T. The Optical Absorption and Photoconductivity Spectra of Hexagonal Boron Nitride Single Crystals. Phys. Status Solidi A 2005, 202, 2229-2233.

# Recommended by ACS

### Symmetry of the Hyperfine and Quadrupole Interactions of Boron Vacancies in a Hexagonal Boron Nitride

Irina N. Gracheva, Marat R. Gafurov, et al.

FEBRUARY 13, 2023

THE JOURNAL OF PHYSICAL CHEMISTRY C

READ

### **Extraordinary Phonon Displacement and Giant Resonance** Raman Enhancement in WSe<sub>2</sub>/WS<sub>2</sub> Moiré Heterostructures

Sharidya Rahman, Yuerui Lu, et al.

NOVEMBER 28, 2022

ACS NANO

READ 🗹

#### Confined Vacuum Resonances as Artificial Atoms with **Tunable Lifetime**

Rasa Rejali, Sander Otte, et al.

JULY 11, 2022

ACS NANO

READ 🗹

# Controlling Spin-Orbit Coupling to Tailor Type-II Dirac

Nguyen Huu Lam, Jungdae Kim, et al.

JULY 15, 2022

ACS NANO

READ

Get More Suggestions >